Full Appendices for the manuscript (updated 2020/10/28)

Appendix-A Setup details, Movies & Animations

1) **Driving** mechanism

The rotating boundary (the upper cone) is driven by stepping motor EzM-56L or EzM-86X (www.fastech.co.kr) with a maximum torque of 1.5 N-m or 12 N-m, respectively, optimized for different experimental conditions. The motor is close-loop controlled and is connected with backlash-free 1/100 or 1/10 speed reducers, making an effective maximal torque in the range of 10^2 N-m that is an order of magnitude higher than the strong fluctuations of torque (shown as Fig.2a in the main texts) and their mean values (Fig.1c and 1d) --- with the same conversion factor stress≡ torque/($2\pi R^3/3$) taken into account. The central shaft is made of stainless steel with a diameter 1cm and the mechanism is reinforced by an L-shaped aluminum rail (4cm-wdie in both directions, shown as in the photograph on the upper right of Fig.-A). For the PDMS particles (See Appendix-C for their elasticity) driven at the maximal density and torque, the angular deflection, if any, is much less than 1/1000 of a rotation (equivalent to ~1/100 in effective shear strain), as we have verified by the classic "optical lever" (using a laser beam and a mirror attached).

The base of the device, coupled with force sensors, is built at the same level of rigidity and is verified the same way. See Sec.2 below.

We have also verified that different versions of sidewalls (the free-sliding rings shown as **Fig.1a** in the Manuscript, versus simply a smooth glass container as shown on the upper left of **Fig.-A** below), do not create significant differences in terms of the fluctuations discussed in this paper.

2) **Sensor** arrangement & Different versions of **sidewalls**

Different generations of the device are built on the same base frame, shown on upper left of Fig.-A. Three sensors below the base are used to determine the normal force (F_z) and two minor torques (along x and y, not discussed). Three other sensors on the x-y plane, are responsible for determining the torque along z and the net force in horizontal directions (F_x and F_y). These physical quantities are depicted in the schematic on the lower left of Fig.-A.

3) **Animation & Movies**

--- see Table in **HTML**.

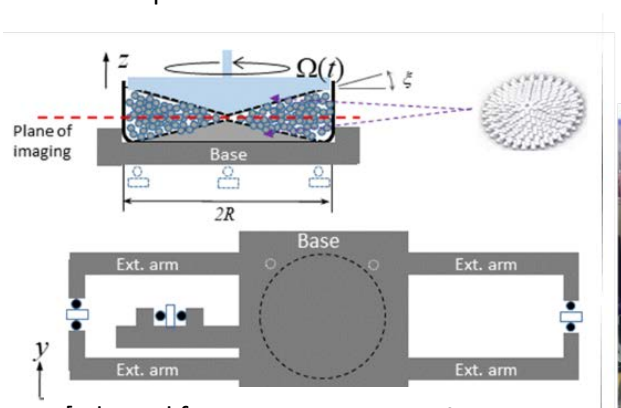

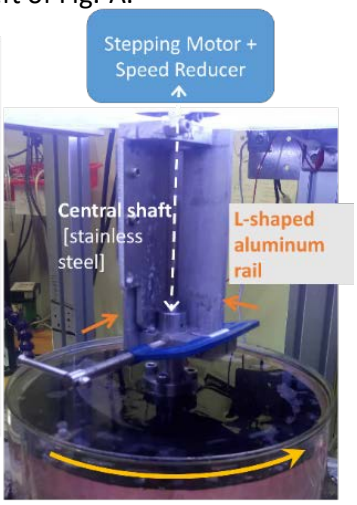

Fig.-A

[adapted from J.-C. Tsai, et al., *Soft Matter*, 2020, DOI: 10.1039/d0sm00405g]

Upper panels
Setup schematics & a close-up photo for the reinforced shaft;

Lower left: schematics for the four physical quantities derived;

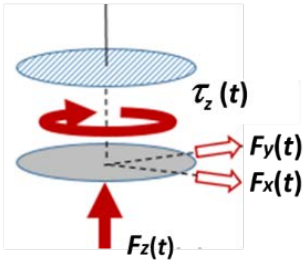

Lower right: 3D stacking of differential images, in sync with τz(t)

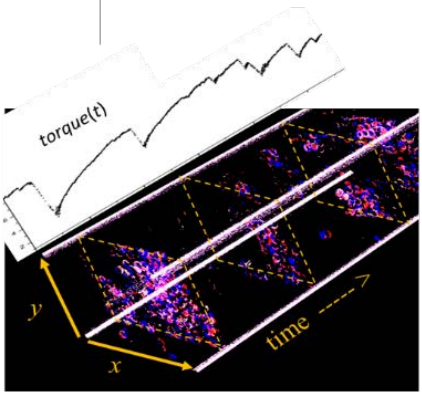

Appendix-B One rudimentary definition of “large drops” (LD) --- regarding #LD/strain on **Fig.1e**

Many prior works have proposed distinctions on “small” avalanches (by localized movements, as our *stick* mode) vs. “large” stress drops (as a system-wised “event”, in our *slip* mode). Although the spatial characterization demands further work, here with *torque signals*, one might choose a reasonable threshold to define “small vs. large”: In addition to identifying the abrupt changes of torque, we have also computed the long-term root-mean-squared (RMS) fluctuations over a large total strain ~O(100) for each steady-state experiment. We believe that measuring a sudden drop against the RMS value should reflect the extent of the avalanche in comparison to the incremental adjustments of the packing accumulated over long time (strain).

For consistency, we choose the scale 2RMS as a threshold for defining a large drop (LD) on **Fig.1e**, as a way to compare data from experiments using different fluids. We have verified that *the “rise and fall”* of the viscous number *J* as the general trend *is insensitive to the choice of this threshold*, despite the absolute values of #LD might change. The rise-and-fall also serves as a good indicator for the “degree of stick-slips”.

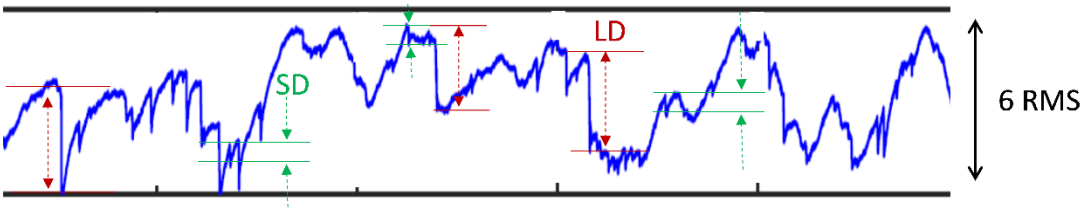

Fig.-B Illustration of time series of torque, using a state between T and β. The scale of 6RMS fluctuation is indicated by the distance between the two thick lines in parallel. Some of the large drops (LD) and small drops (SD) are indicated by dotted arrows pointing outwards and inwards, respectively, based on a threshold of 2RMS.

Appendix-C The making and characteristics of PDMS particles

1) **Molding** of PDMS particles

We mold our PDMS particles. Typically, the mixture of Sylgard-184 (Dow Chemical) with agents A:B = 10:1 (as recommended by its documentation) is vacuumed in room temperature for half an hour before molding, in order to reduce the gas content. Precision-machined acrylic molds in the form of 2D array of hemispheres (typically with d_0=9mm in diameter), with a small hole at the centers of each, are carefully stacked up in the A-B mixture carefully to avoid air pockets. Long screws go through another set of array of larger holes, in order to align and fasten all acrylic layers on to a thick aluminum plate with threaded holes. Most of our samples are cured at around 60 degree-C overnight. The typical batch of particles is in O(1000). See upper left of Fig.-C.

Cured particles are then removed from the mold and inspected individually. Small "rods" at the annex of each hemispheres are trimmed. In cases when fluorescence is needed, we have added to the A-B mixture a small amount of Rhodamine that is dissolved in ethanol alcohol. (Alcohol is soon vaporized before the curing starts).

2) **Hertzian response** & elasticity

By measuring the force (Fz) in response to compression ($|z\text{-}z_0|$), we are able to verify that particles with a wide range of A/B ratios exhibits Hertzian response, but with different elasticities ---- see the right-hand-side of Fig.-C. The data show that, In the case of A/B=10:1, the elastic modulus is about 50 times that of the commercial hydrogel particles (1cm "Magic Balls") commonly used in gardening, decoration, and in our published work [J.-C. Tsai, et al., *Soft Matter*, 2020, DOI: 10.1039/d0sm00405g] as well, exhibiting a Young's modulus ~1.5MPa as have been confirmed by many other research groups[1]. The Poisson ratio ~0.5 is assessed by close-up imaging during the compression.

3) **Stability** of our fluid-immersed PDMS particles **over time**

We are aware that, because of PDMS is porous, therefore immersing them (statically) in fluid can make noticeable changes on their frictions (which in turns affects the "flow curves" and fluctuations) at the time scale of weeks. Therefore, even at exactly the same volume fraction, different batches of samples/experiments can exhibit shifts in the mean stress or the characteristic shear rates of transition (within a factor of two, which is considered small as our investigation over the rate dependence spans over two to three decades of driving rate).

For this reason, *even though our stepping motor can operate stably for weeks*, we have still limited our collection of *steady-state* statistics to three days as the maximum, for which we can verify empirically that the possible slow shifts of frictional properties over time are smaller than the changes we create by changing our driving rates.

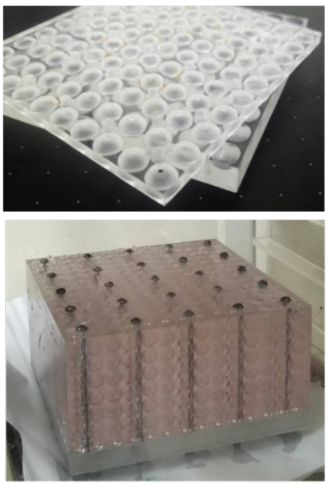

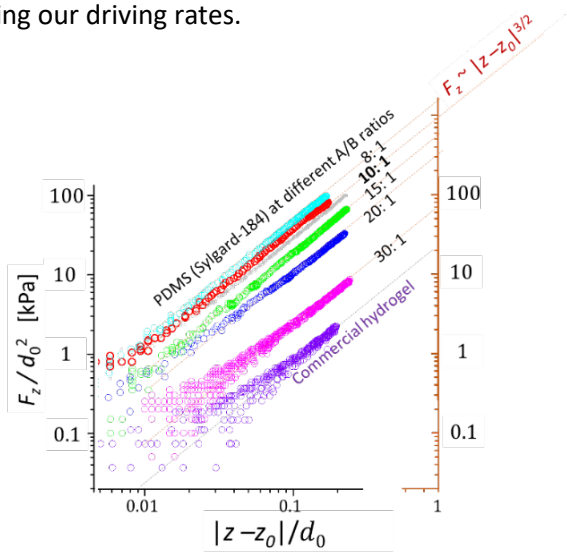

Fig.-C
Left: Photographs of our acrylic molds
Right: Measured Response to compression in z.

Hertzian Law

$$\frac{F_z}{{d_0}^2} \sim \frac{E}{3(1-\nu^2)}\left(\frac{|z_0 - z|}{d_0}\right)^{\frac{3}{2}}$$

[1] https://www.sandia.gov/polymer-properties/E1-Youngs_modulus.html ; http://niml.org/wiki/index.php?title=Quantification_of_the_Modulus_of_Elasticity_and_Dynamic_Properties_of_Sylgard_for_Various_Mixing_Ratios,_2003-2006

Appendix-D CDF vs PDF, and the stronger-than-exponential truncation

Two conventions on the presentation of "event statistics" have long existed in the research community. For the same set of data (for our state-T), we present the **cumulative distribution function** (CDF, bin-size independent) on the left of Fig.-D, and that can also be translated into a **probability density function** (PDF, bin-size dependent) on the right. Note the difference in the power-law (PL) exponent.

In addition, the data of state-T show a significant deviation from PL at large values in both CDF and PDF. Many prior works (such as item 1 in Additional REFERENCEs) have presented such "truncation" using "**compensated plots**", by plotting the statistical counts multiplied by the inverse of best fit to PL, to visualize the form of truncation. In the lower part of Fig.-D, we show with log-linear plots that both the CDF and PDF exhibit a truncation that is substantially "stronger than exponential".

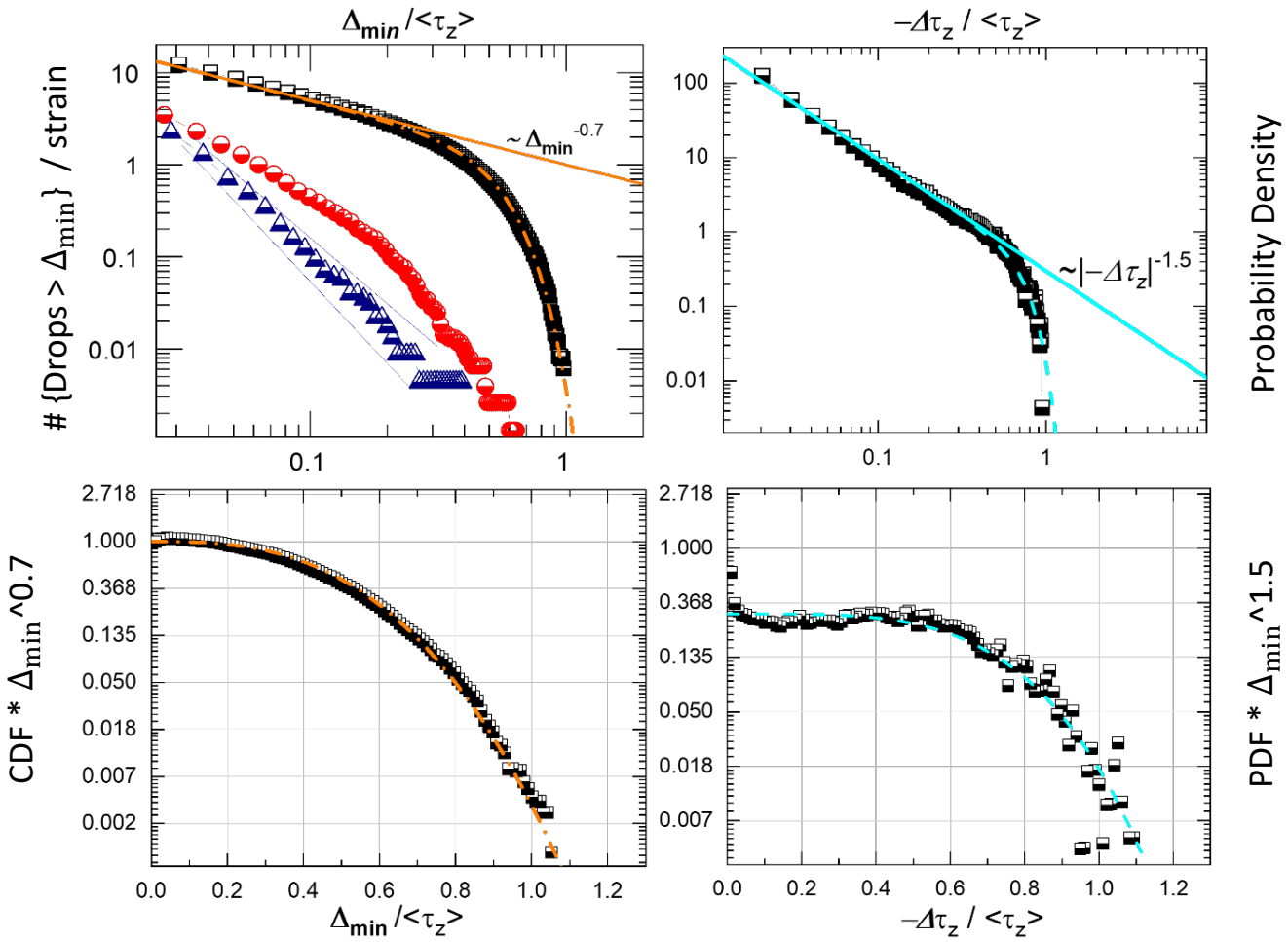

Fig.-D CDF vs PDF, and "compensated plot" for both.
Upper Left: CDF adapted from the inset of Fig.2a in the main Manuscript. Black squares stand for data of state-T, which is translated to PDF on the **Upper Right**.
Lower panels: "**Compensated plots**" based on CDF (with data multiplied by X^0.7) and PDF (with data multiplied by X^1.5), respectively, where X stands for the horizontal coordinate of each graph. Note the log-linear scale, on which an exponential function would have been represented by a straight line. We show that the truncation is stronger-than-exponential in either case: The dashed line represents a hypothetical curve of exp{-(X/0.54)^2.8} on the left and 0.3*exp{-(X/0.77)^4} on the right,.

Appendix-E Use of ϕ in place of *confining pressure*, for the Phase Diagram

From an experimental point of view, it is convenient to use ϕ and the dimensionless shear speed as the two control parameters in expressing our Phase Diagram Fig.3c, although the connection with viscous number J would be lost because the data no longer incorporate information of the confining stress (σ_N).

Nevertheless, this is advantageous in delivering an empirical fact: Based on our additional experiments with precision-density matching, we have found that at ϕ=0.48 and below, σ_S increases monotonically with the shear rate imposed. At ϕ=0.48, $\sigma_S(\dot{\gamma})$ has a nearly flat part at slow shear rate, followed by a rise with a steeper logarithmic slope (but still < 1) at higher shear rates. Further lowering the volume fraction makes the data go straight on the log-log plot ---- see our published work [J.-C. Tsai, et al., *Soft Matter*, 2020, DOI: 10.1039/d0sm00405g , Fig.1c]. Such similarity to the behaviors of frictionless particles might be interpreted as the consequence of becoming a fully suspended flow (SF), in which all inter-particle collisions are brief and do not allow sufficient time of contact for the tribology to take effect --- even if the tribology is still speed-dependent.

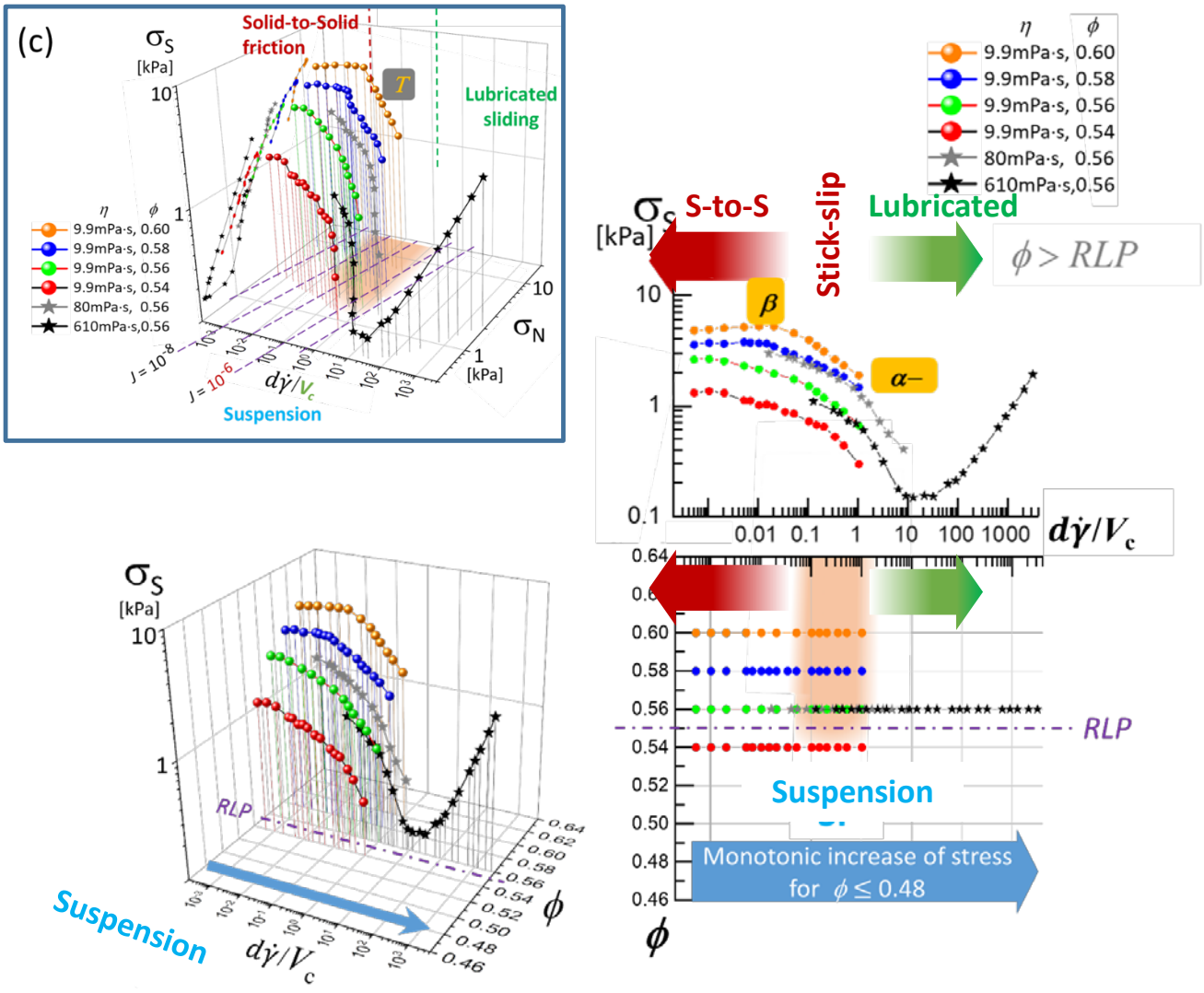

Fig.-E Alternative representations of Fig.3c (upper left, adapted from the main Manuscript), using volume fraction ϕ in place of the normal stress σ_N

Appendix-F Side-by-side comparison to BDH model [8]

In 2011, Ben-Zion, Dahmen, and Uhl (BDH) put forth a unifying phase diagram for sheared solids with two tuning parameters, which is a generalization from a single-parameter analytical theory earlier by the same group of authors.[10]

The interpretation of our phase diagram have certain overlaps with the BDH model in the vocabularies we use. However, there are substantial differences, as compared below.

[Similarities]
------- We have the same number of material parameters, namely (1) a characteristic velocity V_c determined by inter-particle tribology and (2) the friction coefficient (at the slow-limit), as those in the BDH model: (1) the weakening parameter ε and (2) the cohesive healing rate/time.
------- We have the same number of control variables, namely (1) an imposed shearing speed $d\dot{\gamma}$ and (2) volume fraction ϕ, as those in the BDH model: (1) the shear rate $\dot{\gamma}$ and the (2) void fraction $\nu \equiv (1-\phi/\phi_{Max})$.

[Differences]
--------In BDH model, granular materials (GM) are seen as a non-cohesive limit, namely Q = $\dot{\gamma}$/(healing rate) approaching zero. This equivalent to a "static limit", namely $\dot{\gamma} = 0$. It is only natural that GM in this model would not exhibit rate dependence.
--------We recognize the fact that "jamming density" (the ϕ_{Max} in BDH) cannot be an independent parameter as it depends on friction and is therefore influenced by the driving rate.

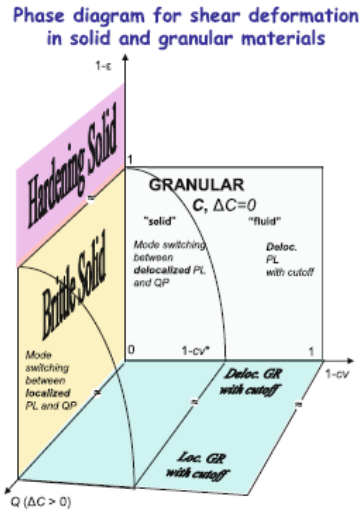

Fig.-F: BDH phase diagram, adapted from the original paper [8]

Therefore, even though we also choose to neglect the small cohesiveness between PDMS particles in the regimes we are considering, it is the very existence of the characteristic speed V_c that produces the rate dependence and the rich phase diagram (Fig.3c and Appendix-E). Meanwhile, we have determined the V_c (and the associated "velocity weakening") by direct measurement (Fig.3b).

It is worth pointing out that our "tribology" between PDMS surfaces is determined entirely by how the tangential force between particle surfaces depends on the sliding speed. We do not intend to distinguish the *microscopic* "stick" and "slip" as BDH model does in defining their weakening parameter ε as a local property. (In our manuscript, we refer to "stick-slips" as the mode switching behavior from a *macroscopic* point of view: Stress builds up during the "stick" mode with only sporadic local avalanches, until the system switches to "slip" mode featured by a sudden drop with a cascade of events all within a short time. Such MS repeats itself, in response to the global shearing that is imposed by the steady motion of the boundary.)

Although we do not think our interpretation is the only possibility that fits the phenomenology, the picture we offer seems to give a coherent explanation on what we observe: The speed-dependent tribology between fluid-lubricated soft particles "blurs" the jamming, so that such transition it is no longer determined solely by the packing fraction ϕ alone (as it seems to be for "hard spheres").

Additional REFERENCEs

(1) Denisov, D. V.; Lörincz, K. A.; Uhl, J. T.; Dahmen, K. A.; Schall, P. Universality of Slip Avalanches in Flowing Granular Matter. *Nat. Commun.* **2016**, *7* (1), 10641. https://doi.org/10.1038/ncomms10641

(2) Antonaglia, J.; Wright, W. J.; Gu, X.; Byer, R. R.; Hufnagel, T. C.; LeBlanc, M.; Uhl, J. T.; Dahmen, K. A. Bulk Metallic Glasses Deform via Slip Avalanches. *Phys. Rev. Lett.* **2014**, *112* (15), 155501. https://doi.org/10.1103/PhysRevLett.112.155501.

(3) Guazzelli, É.; Pouliquen, O. Rheology of Dense Granular Suspensions. *J. Fluid Mech.* **2018**, *852*, P1. https://doi.org/10.1017/jfm.2018.548.

(4) Nicolas, A.; Ferrero, E. E.; Martens, K.; Barrat, J.-L. Deformation and Flow of Amorphous Solids: Insights from Elastoplastic Models. *Rev. Mod. Phys.* **2018**, *90* (4), 045006. https://doi.org/10.1103/RevModPhys.90.045006.

(5) Jensen, H. J. *Self-Organized Criticality: Emergent Complex Behavior in Physical and Biological Systems*; Cambridge University Press, 1998.

(6) Liu, C.; Ferrero, E. E.; Puosi, F.; Barrat, J.-L.; Martens, K. Driving Rate Dependence of Avalanche Statistics and Shapes at the Yielding Transition. *Phys. Rev. Lett.* **2016**, *116* (6), 065501. https://doi.org/10.1103/PhysRevLett.116.065501.

(7) DeGiuli, E.; Wyart, M. Friction Law and Hysteresis in Granular Materials. *Proc. Natl. Acad. Sci.* **2017**, *114* (35), 9284–9289. https://doi.org/10.1073/pnas.1706105114.

(8) Ben-Zion, Y.; Dahmen, K. A.; Uhl, J. T. A Unifying Phase Diagram for the Dynamics of Sheared Solids and Granular Materials. *Pure Appl. Geophys.* **2011**, *168* (12), 2221–2237. https://doi.org/10.1007/s00024-011-0273-7.

(9) Wright, W. J.; Long, A. A.; Gu, X.; Liu, X.; Hufnagel, T. C.; Dahmen, K. A. Slip Statistics for a Bulk Metallic Glass Composite Reflect Its Ductility. *J. Appl. Phys.* **2018**, *124* (18), 185101. https://doi.org/10.1063/1.5051723.

(10) Dahmen, K. A.; Ben-Zion, Y.; Uhl, J. T. Micromechanical Model for Deformation in Solids with Universal Predictions for Stress-Strain Curves and Slip Avalanches. *Phys. Rev. Lett.* **2009**, *102* (17), 175501. https://doi.org/10.1103/PhysRevLett.102.175501

.